Variable-Gear EV Reluctance Synchronous Motor Drives—An Evaluation of Rotor Structures for Position-Sensorless Control

Wikus T. Villet, *Student Member, IEEE*, and Maarten J. Kamper, *Senior Member, IEEE*

***Abstract*—The reluctance synchronous motor (RSM) is identified to be well suited for the variable-gear (VG) electric vehicle (EV) drive. It is shown in this paper, however, that the RSM drive's position-sensorless capability is limited at zero or very small current magnitudes due to a limited saliency magnitude. In this paper, a novel epoxy–resin-casted rotor with no iron ribs is proposed to increase the saliency of the RSM at zero reference current. This rotor RSM is simulated in finite-element (FE) analysis, built, evaluated, and compared with conventional flux barrier rotor RSMs. The effect of rotor skewing on the position-sensorless control (PSC) capability of the RSM is also evaluated by means of FE analysis and measurements. Other performance aspects are also considered in this paper. It is concluded that, overall, the skewed epoxy–resin-casted rotor RSM drive has no PSC problems in the entire load and speed regions and is well suited for VG EV drives.**

***Index Terms*—Position-sensorless control (PSC), reluctance synchronous machines, variable-speed drives.**

NOMENCLATURE

Symbols:

u, i, ψ	Voltage, current, and flux linkage.
r, L	Resistance and inductance.
θ_e, ω_e	Electrical-rotor angle and speed.
Δ, Σ	Difference and sum.
ΔL	Inductance saliency.
L_Δ	Secant (instantaneous) saliency.
ψ_Δ	Fundamental saliency.
P_{in}, P_m	Input and shaft power.
P_{loss}, η	Losses and efficiency.

Indices:

s, r	Stator and rotor.
α, β	Stator-fixed Cartesian axes.
d, q	Rotor-fixed direct and quadrature axes.
c	Carrier frequency.
$\sim$	Secant (instantaneous) values.

Scalar values are written in normal letters, e.g., R or τ. Vector values are written in small bold letters, e.g., $\boldsymbol{i}$ or $\boldsymbol{\psi}$. Subscripts describe the location of the physical quantity, e.g., r_s is the stator resistance. Superscripts specify the reference frame of the quantity, e.g., $\boldsymbol{i}_s^r$ is the stator current vector in the rotor reference frame. Estimated quantities are indicated with a hat, e.g., $\hat{\theta}_e$. The matrix $\boldsymbol{J}$ is the equivalent complex operator j and is used for orthogonal rotation.

I. INTRODUCTION

MOST OF THE world's large automotive companies are investing in hybrid electric and electric vehicles (EVs). EV drives are usually implemented with fixed-gear (FG) transmissions. The studies in [1]–[4] show that variable-gear (VG) EVs operate more optimally on the drive cycle efficiency map than FG EVs. A VG EV drivetrain could thus result in an increased vehicle range. Another advantage of a drivetrain with a VG is the possibility of using a downsized motor [1]. With FG EV drives, the power performance of the vehicle strongly depends on the constant power speed range of the motor; hence, another advantage of a VG drivetrain is that machines with limited constant power speed range can be considered as an alternative to permanent magnet (PM) machines.

It is shown in [5] that reluctance synchronous motors (RSMs) with a high L_d/L_q ratio have good constant power speed range performance. RSM's with low L_d/L_q ratios, however, have limited constant power speed range performance; hence, these machines are not suited for an FG EV drivetrain. The studies in [6] and [7] have shown that the efficiency of the RSM, within its rated speed range, is comparable with that of the induction machine (IM), if not better. The RSM is thus well suited for non-PM VG EV drives. A VG RSM EV drivetrain has the potential to be compact and cheap with a small motor.

Position-sensorless control (PSC) at all operating points is an absolute requirement for EV drives, even if used as backup in conjunction with a low-resolution position sensor. Rotating high frequency (HF), alternating HF, and arbitrary injection methods are saliency-based PSC methods and are mainly used to estimate the electrical angle of salient pole machines at standstill and low speeds. The studies in [8] and [9], however, show that the phenomena of saturation and saliency shift limit the PSC ability of PM machines under loaded conditions when controlled with saliency-based PSC methods. In this paper, the RSM with a transverse laminated rotor with lateral flux barriers and iron ribs is investigated to see if the aforementioned limitations are also present in position-sensorless controlled RSM drives [10]. The saliency-based PSC capability of the

Manuscript received April 25, 2013; revised August 21, 2013; accepted September 4, 2013. Date of publication November 19, 2013; date of current version May 2, 2014.

The authors are with the Department of Electrical and Electronic Engineering, University of Stellenbosch, 7599 Stellenbosch, South Africa (e-mail: wtvillet@gmail.com).

Color versions of one or more of the figures in this paper are available online at http://ieeexplore.ieee.org.

Digital Object Identifier 10.1109/TIE.2013.2288231

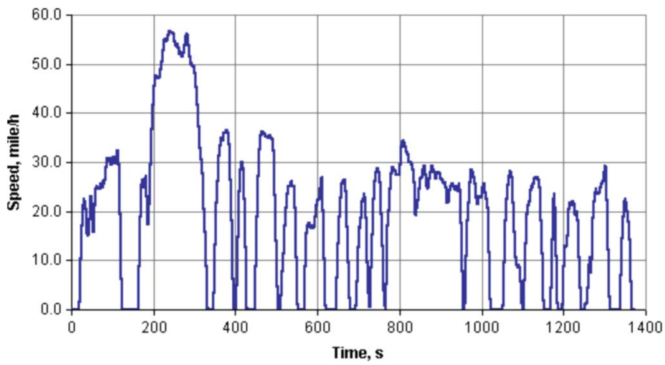

Fig. 1. UDDS for 12.07 km [12].

RSM drive at zero is also evaluated in this paper. It must be emphasized that if the PSC of the RSM drive fail, then the RSM cannot be seen as a viable drive motor for VG EV drives.

Finite-element (FE) analysis and measurements are used in this paper to compare, in terms of saliency-based PSC capability, three RSM drives with three different transverse laminated rotor structures at zero reference current. Also, in this paper, the effect of full slot pitch rotor skew on the PSC capability of the RSM drive is investigated by means of FE analysis and measurements.

One lingering question that still exists regarding PSC is if there is any sacrifice in the efficiency of the drive when compared with the sensor-controlled drive. To investigate this question, the efficiencies of three RSM drives with different rotor structures are evaluated when controlled with and without a position sensor [11]. Finally, the position estimation error of a fundamental saliency PSC method is evaluated to determine if there is any performance difference with the different rotor structures.

II. Urban Dynamometer Drive Schedule and Load

The urban dynamometer driving schedule (UDDS) is a dynamometer test on fuel economy in urban driving conditions. The test simulates an urban route of 12.07 km in Fig. 1 [12]. This UDDS is used to better understand performance expectations of an EV on urban roads. Fig. 1 shows various instances where the vehicle is at constant speed or accelerating, as expected. Surprisingly, however, the UDDS also reveals that there are various instances where the vehicle stands still or coasts where no torque is required. It is important that all driving conditions, including standstill and coasting, are investigated to improve the performance of EVs. In the rest of this paper, the focus is on evaluating the performance of a position-sensorless-controlled VG RSM EV drive with regard to the UDDS.

III. PSC of RSM Drives

Various hybrid PSC methods exist where two PSC methods are combined to control synchronous machines without a position sensor in the entire rated speed range, to name only a few, [13]–[17]. An HF injection PSC method is combined with an active flux method in [13], and in [16] and [17], it is combined with a back-EMF method. The hybrid PSC method used in this evaluation also utilizes a simplified alternating HF injection method at standstill and low speeds (Section III-A) and a fundamental saliency PSC method at medium to high speeds (Section III-B) [18].

A. Alternating HF Injection Method

The alternating HF injection method makes use of an amplitude modulation scheme to track the electrical angle of the RSM by superimposing an HF voltage vector onto the fundamental control voltage vector in the estimated rotary reference frame [19]. With proper demodulation, it is possible to track the anisotropy position which rotates at the same angular frequency as the rotor [20]. Under HF excitation, the RSM stator voltage equation consists of only an inductance term as in (1) [19], [21]

$$\boldsymbol{u}_{\mathrm{sc}}^{(r)} = \boldsymbol{L}^{(r)} \frac{d\boldsymbol{i}_{\mathrm{sc}}^{(r)}}{dt} \tag{1}$$

$$L_d = \frac{\partial \psi_d}{\partial i_d} \quad L_q = \frac{\partial \psi_q}{\partial i_q}. \tag{2}$$

The tangential inductances are calculated with (2) and make up the matrix $\boldsymbol{L}^{(r)}$ [21]. Superscript r denotes the quantity in the rotary reference frame. Subscript s indicates stator quantities. The injected carrier voltage vector is as defined in (3) when implementing alternating HF injection PSC. The demodulated stator current in the estimated rotary reference frame (as dissipated by superscript $\hat{r}$) is shown in (4) [21]

$$\boldsymbol{u}_{\mathrm{sc}}^{(\hat{r})} = \begin{bmatrix} u_c \cos(\omega_c t) \\ 0 \end{bmatrix} \tag{3}$$

$$\boldsymbol{i}_{s(\mathrm{demod})}^{(\hat{r})} \approx \frac{u_c}{2L_d L_q \omega_c} \left(L_\Sigma \begin{bmatrix} 1 \\ 0 \end{bmatrix} - \Delta L \begin{bmatrix} 1 \\ 2\Delta\theta_e \end{bmatrix} \right) \tag{4}$$

where

$$L_\Sigma = \frac{(L_d + L_q)}{2} \qquad \text{and} \qquad \Delta L = \frac{(L_d - L_q)}{2}. \tag{5}$$

L_Σ is the mean inductance, and ΔL is the inductance saliency (difference inductance). $\Delta\theta_e = \theta_e - \hat{\theta}_e$ is the electrical position estimation error. Equation (4) shows that the q-axis current has information regarding the position estimation error. The q-axis current can be used to drive a phase-locked loop (PLL) to track the electrical rotor angle [20], [21]. Furthermore, (4) shows that the electrical position estimation error is scaled by the magnitude of the inductance saliency. This implies that it will be impossible to track the electrical angle if $L_d = L_q$.

B. Fundamental Saliency Method

The RSM does not have a back EMF; thus, conventional back-EMF methods cannot be used as PSC. A fundamental saliency PSC method for medium to high speeds is proposed in [22]. The flux linkage vector can be calculated with the secant (instantaneous) inductance defined as in (6), assuming that the flux linkage vector is linearly dependent on the current vector. These inductance values are different from those which are calculated with (2). With this assumption, it is possible to describe the stator flux vector in the stationary reference frame by (7) [22], where L_Δ is the secant (instantaneous) inductance saliency and equal to $(\tilde{L}_d - \tilde{L}_q)/2$

$$\boldsymbol{L} = \frac{\boldsymbol{\psi}_s^{(s)}}{\boldsymbol{i}_s^{(s)}} \tag{6}$$

$$\begin{aligned}\boldsymbol{\psi}_s^{(s)} &= L_\Sigma \boldsymbol{i}_s^{(s)} + L_\Delta \begin{bmatrix} \cos(2\theta_e) & \sin(2\theta_e) \\ \sin(2\theta_e) & -\cos(2\theta_e) \end{bmatrix} \boldsymbol{i}_s^{(s)} \\ &= \boldsymbol{\psi}_\Sigma^{(s)} + \boldsymbol{\psi}_\Delta^{(s)}. \end{aligned} \tag{7}$$

It is shown in [22] that the fundamental saliency, ψ_Δ can be calculated with measurable quantities. It is also shown in [22] that it is possible to calculate the fundamental saliency with (8) in the estimated reference frame as $\hat{\psi}_\Delta$, with the estimated electrical angle $\hat{\theta}_e$. An angle difference between the two vectors $\boldsymbol{\psi}_\Delta^{(s)}$ and $\hat{\boldsymbol{\psi}}_\Delta^{(s)}$ can be calculated by taking the vector product as in (9) [22]. This angle is equal to the position estimation error $\Delta\theta$ and can be fed back to a PLL, which is a PI controller that will drive the error to zero [22]

$$\hat{\boldsymbol{\psi}}_\Delta^{(s)} = L_\Delta \begin{bmatrix} \cos(2\hat{\theta}_e) & \sin(2\hat{\theta}_e) \\ \sin(2\hat{\theta}_e) & -\cos(2\hat{\theta}_e) \end{bmatrix} \boldsymbol{i}_s^{(s)} \tag{8}$$

$$\begin{aligned}\Delta\theta_e &= \boldsymbol{\psi}_\Delta^{(s)\,\mathrm{T}} \boldsymbol{J} \hat{\boldsymbol{\psi}}_\Delta^{(s)} \\ &= \left|\boldsymbol{\psi}_\Delta^{(s)}\right| \left|\hat{\boldsymbol{\psi}}_\Delta^{(s)}\right| \sin(2\Delta\theta_e). \end{aligned} \tag{9}$$

IV. Degradation of Saliency-Based PSC Performance

According to [8] and [23], there are two effects that can distort the PSC capability of PM drives when controlled with a saliency-based PSC method, namely, saturation and cross-coupling effects. During saturation, the magnitude of the inductance saliency ΔL decreases as the flux saturates within the machine until PSC is not any longer possible. This saturation effect occurs when the machine is loaded.

It is found that cross-coupling between the d- and q-axes results in a mutual inductance term L_{dq} and is caused by the asymmetrical saturation of the rotor [9]. To investigate the distortion caused by the cross-coupling effect in RSMs, three rotor structures, as shown in Fig. 2, are simulated in the JMAG FE package. To adhere to convention, as given in [8], these three rotor structures are referred to as the ideal [Fig. 2(a)], lateral-rib [Fig. 2(b)], and central-rib [Fig. 2(c)] rotors. The flux density maps of Fig. 2(a) and (b) at rated conditions are similar and symmetrical, as also identified by Bianchi and Bolognani [8]. However, high distortion is present in Fig. 2(c), where the flux lines concentrate in the central rib, causing asymmetrical saturation and thus increasing the cross-coupling between the d- and q-axes. If the concentration on the central rib is high enough, it can cause the PSC method to misalign with the d-axis of the rotor. This phenomena is referred to as saliency shift in [24] and [25]. The saliency shift of the synchronous machine can be calculated as follows [26]:

$$\gamma = \arctan\left(\frac{L_{\mathrm{dq}}}{\Delta L}\right). \tag{10}$$

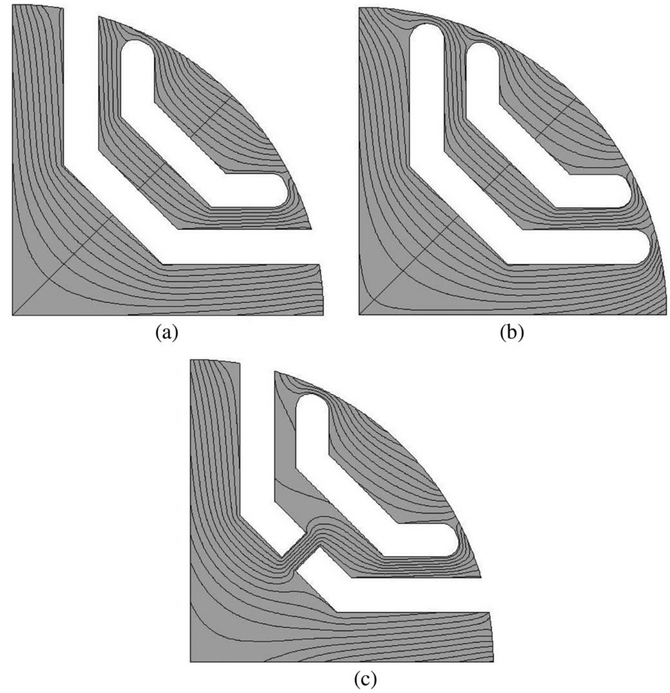

Fig. 2. Cross-coupling effect on (a) the ideal, (b) lateral-rib, and (c) central-rib rotor RSM structures. (a) Ideal. (b) Lateral rib. (c) Central rib.

TABLE I
Parameters of the Lateral-Rib Rotor RSM Drive

Pole pairs	2
Number of stator slots	24
Stator outer diameter	65 mm
Rotor outer diameter	37.5 mm
Active rotor stack length	131 mm
Phase resistance	3.4 Ω
Rated line-line voltage	400 V
Rated phase current	3.5 A (RMS)
Rated frequency	50 Hz
Rated power	1.14 kW
Rated torque	7.25 Nm
Nm/L	16.68
Switching frequency	5 kHz
Sampling frequency	10 kHz
DC bus voltage	565 V

V. Evaluation of the Lateral-Rib Rotor RSM Drive

An RSM with an unskewed lateral-rib rotor configuration, as in Fig. 2(b), is used as a benchmark to further evaluate the PSC capabilities of RSM drives. The investigated RSM has a standard three-phase distributed winding IM stator. The details of this machine are listed in Table I.

The RSM is a salient pole machine $(L_d \neq L_d)$, making it ideal for saliency-dependent PSC methods. To prove this, 2-D FE and measured analyses are done on the RSM to investigate its position-sensorless capability. Only the resistance of the end-winding inductance is taken into account in the simulation package. The simulated flux linkages are used to calculate the tangential inductances with (2). Both the d- and q-axis flux linkages are functions of both i_d and i_q [8]. If (2) is used as in (11) to calculate the tangential inductance, it is possible to

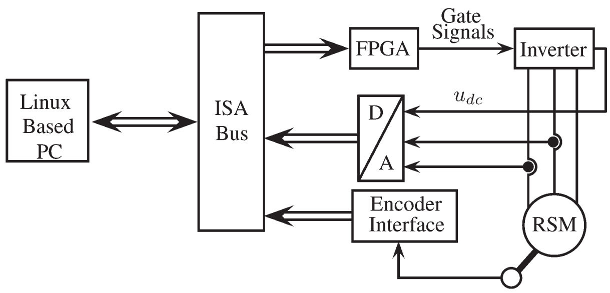

Fig. 3. Rapid prototype controller used as part of a test bench.

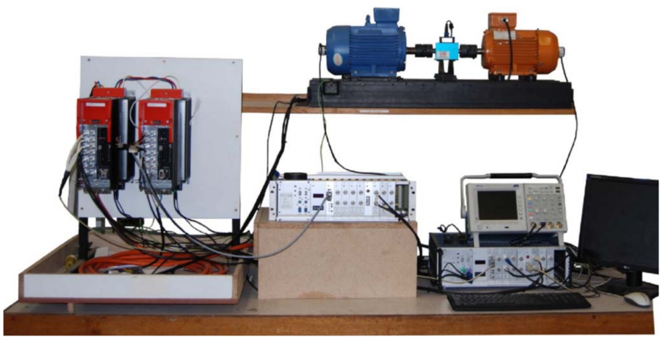

Fig. 4. Test bench used with an IM (left) drive as load to evaluate the three RSM (right) drives.

investigate the saliency of the RSM with regard to the geometry of the design, minimizing the cross-coupling effects

$$L_d = \frac{\Delta\psi_d}{\Delta i_d}, \qquad \psi_d(i_d, 0)$$
$$L_q = \frac{\Delta\psi_q}{\Delta i_q}, \qquad \psi_q(0, i_q). \tag{11}$$

The inductance saliency of the lateral-rib rotor RSM is also measured to compare with the FE results. A rapid prototype system (RPS), as shown in Fig. 3, is used for measured evaluations. The RPS consists of a LINUX-based PC which is connected via an ISA bus to an FPGA, analog-to-digital converter, and encoder interface. Field-oriented control is implemented with PI current controllers. The test bench is as shown in Fig. 4. The RSM is connected via a torque sensor to an IM. Two dc-linked inverters, each with a dedicated RPS, are used to drive each machine.

The frequency of the IM is kept at 50 Hz by the RPS for flux linkage measurements. The voltage equation of the RSM in the rotary reference frame is as shown in (12). The current in the rotary reference frame is kept constant with PI controllers; thus, it can be assumed that the flux linkage of the RSM is also constant in the rotary reference frame. The flux linkage derivative term in (12) thus falls away. The flux linkage of the RSM is then calculated with (13). The calculated flux linkage values are stored on the LINUX-based PC. These values are used offline with (11) to calculate the measured inductance curve as a function of current

$$\boldsymbol{u}_s^r = r_s \boldsymbol{i}_s^r + \dot{\boldsymbol{\psi}}_s^r + \boldsymbol{J}\omega_e \boldsymbol{\psi}_s^r \tag{12}$$
$$\boldsymbol{\psi}_s^r = \boldsymbol{J}^{-1} \frac{\boldsymbol{u}_s^r - r_s \boldsymbol{i}_s^r}{\omega_e}. \tag{13}$$

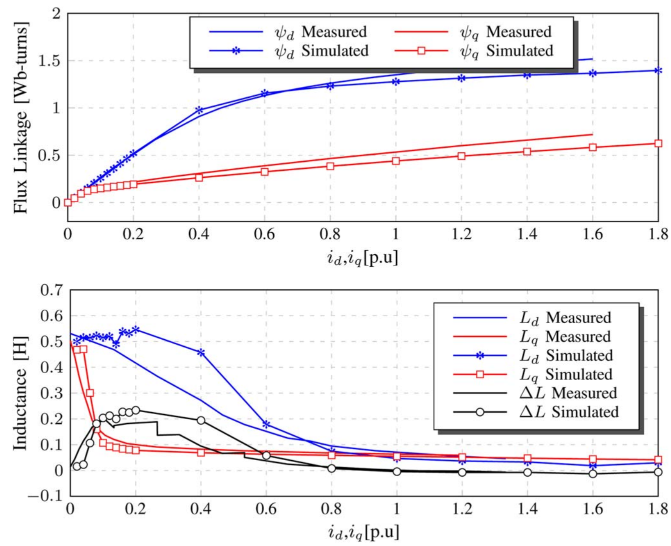

Fig. 5. Measured flux linkages and inductances versus simulated results of the lateral-rib rotor configuration.

The results of the simulated and measured analyses of the lateral-rib rotor structure are shown in Fig. 5. The first frame shows the uncoupled flux linkages as a function of current, and the second frame shows the tangential inductances. It is clear that there are some irregularities between the measured and simulated results. This might be due to an uncertainty regarding the rotor and stator steel. Distortion is also visible in the inductance profile as a combined result of discrete measurements (at certain setpoints) and the partial derivative of the flux linkage calculation. This implies that slight gradient deviation of the flux linkage causes large deviations of the inductance. The important aspect regarding this comparison is that the shape of the flux linkages of the measured and simulated results are satisfactorily similar.

Two important results are observed in the measured and simulated inductance saliency (ΔL) shown in the second frame frame of Fig. 5.

1) The magnitude of ΔL decreases as the load increases until PSC is not possible. This is due to the saturation of the flux within the machine, as identified in [8] and [23].
2) $L_d \approx L_q$ at near-zero current magnitudes. This results in ΔL being too small for PSC.

The effects of these two problem areas play a large role in the performance of the position-sensorless controlled drive. The maximum torque of the position-sensorless controlled drive is limited due to the saturation under loaded conditions.

The limited saliency at zero and small current magnitudes also prevents the PSC method from tracking the electrical angle. It is possible, however, to estimate the electrical angle by choosing the current vector in such a way that $i_q \neq 0$ to saturate the q-axis magnetic circuit. It is found that the minimum q-axis current necessary is 0.2 p.u. Although effective, this method is not energy efficient due to the current vector not always following the maximum torque per ampere locus. This method of course also implies that there is always current in the machine even at standstill under no load.

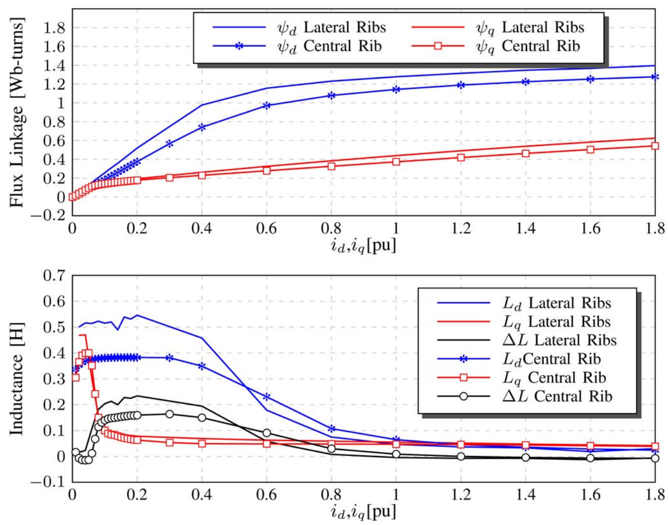

Fig. 6. Simulated flux linkages and inductances of the lateral-rib rotor configuration versus the central-rib rotor configuration (unskewed).

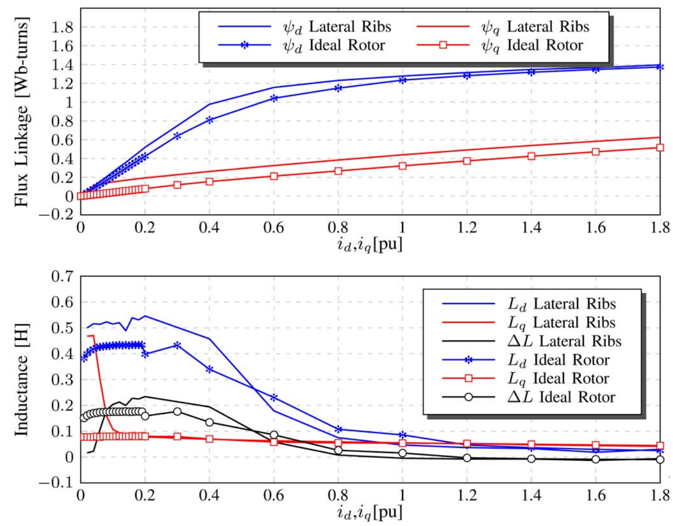

Fig. 7. Simulated flux linkages and inductances of the lateral-rib configuration versus the ideal rotor configuration.

It is shown in Section II that there are various instances of an EV's urban drive cycle where no torque will be required. No torque implies that the reference current will be zero. It is thus clear that the position-sensorless controlled lateral-rib RSM drive will not operate at maximum efficiency if implemented in a VG EV.

VI. Evaluation of the Central-Rib and Ideal Rotor RSM Drives

The problems of flux saturation and saliency shift, with regard to PSC, have already been addressed for PM machines with proposed solutions [8], [9], [23]–[25], [27]–[29]. The problem of limited inductance saliency at very small current vectors are also identified by [26] but no solution to this problem exists yet.

Although, as discussed in the previous section, the central-rib rotor in Fig. 2(c) suffers from saliency shift, this structure is investigated as an alternative to the lateral-rib rotor RSM for high-inductance saliency at zero reference current. The central-rib rotor RSM is also simulated unskewed in order to compare it with the lateral-rib rotor RSM. Fig. 6 compares the simulated uncoupled flux linkages and inductances of the lateral- and central-rib rotor RSM drives. The simulation results show that the central-rib rotor RSM drive also suffers from a lack of saliency at no load.

The second investigated configuration is that of the ideal rotor structure in Fig. 2(a). Again, this configuration is simulated with the rotor configuration unskewed. The FE simulation results of the uncoupled flux linkages and inductances of the ideal rotor are compared with the simulation results of the lateral-rib rotor configuration in Fig. 7. This graph shows that $\psi_d(i_d, 0)$ and $\psi_q(0, i_q)$ have different gradients at already very small current magnitudes, resulting in a high saliency at very low currents. Not only does this configuration have a large saliency magnitude at zero current, it also has a more constant saliency magnitude up to 0.4 p.u and is slightly better than the lateral-rib rotor RSM up to 1.2 p.u. These results suggest that

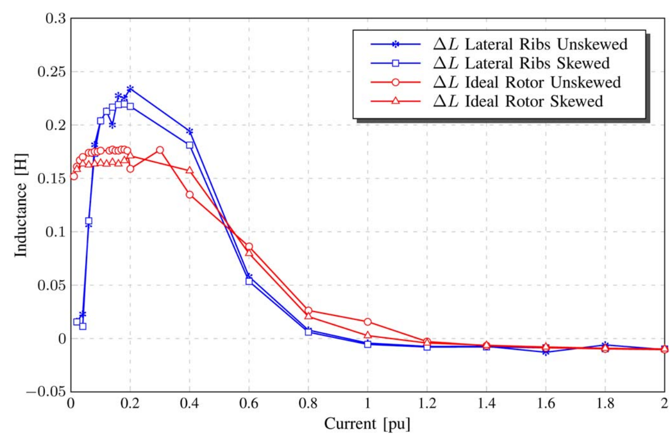

Fig. 8. Simulated inductance saliency comparison of the skewed and unskewed lateral-rib and ideal rotor configurations.

the geometry of the ideal rotor configuration has, as expected, a higher saliency at very small currents than that of the other two configurations.

VII. Skewing of the Rotor

In [27], the effect of skewing of a PM machine on its PSC capability is investigated. The rotor is skewed a quarter of a slot pitch in [27], and the findings are that skewing has little or no effect on the PSC capability of the machine. It is important to investigate the PSC capability of the RSM with the rotor skewed one stator slot pitch. Skewing the rotor one stator slot pitch reduces the torque ripple of the machine. Both the lateral-rib and ideal rotor configurations are simulated in five skewed submachines to simulate a full slot pitch skewed rotor. The saliency acquired from the simulation results is shown in Fig. 8. These results show that there is very little deviation of the saliency when an RSM rotor is skewed one stator slot pitch and that it possesses all the necessary characteristics for successful PSC.

(a) (b)

Fig. 9. Constructed unskewed ideal rotor configuration. (a) CAD sketch of proposed RSM rotor laminations. (b) Epoxy-filled unskewed ideal rotor with ribs removed.

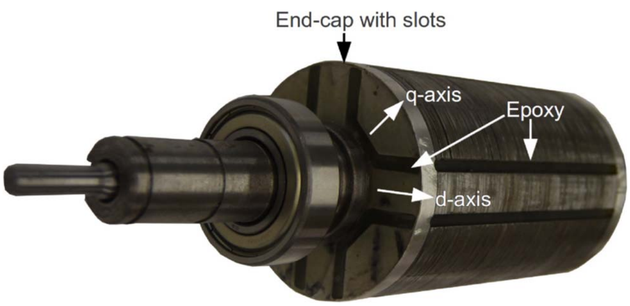

Fig. 10. Unskewed ideal rotor view from top.

VIII. Ideal Rotor Configuration

A. Construction of the Ideal Rotor Configuration

Simulation results suggest that the unskewed and skewed ideal rotor RSM configurations will perform well with PSC at zero reference current. To confirm this statement, we decided to build the unskewed and skewed ideal rotors and evaluate the PSC capability of these RSM drives. The obvious problem is that a piece of the rotor steel "floats" in the air, as shown in Fig. 2(a). To overcome this problem, a novel solution is implemented. Slots that match the flux barriers of the rotor laminations are cut into one of the end caps of the rotor. This makes it possible to fill the axial length of the rotor with epoxy to form an epoxy cast. Epoxy is very strong but not recognized as an adhesive substance; thus, it will not be able to hold the floating piece of iron in place. To take advantage of the strength of the epoxy cast, small cutouts and iron snags are laser cut into the laminations, as shown on the CAD design in Fig. 9(a). These cutouts help the epoxy to grip the floating piece of iron and prevent it from moving away. After allowing the epoxy to harden, a lathe is used to cut out the ribs. The unskewed rotor without its lateral ribs is shown in Fig. 9(b). The end cap which is used to fill the rotor with epoxy is visible in the final result in Fig. 10. The "floating" q-axis is also visible in Fig. 10.

The two constructed rotors are tested in the same stator as the lateral-rib rotor RSM structure on a test bench, as shown in Fig. 4.

B. Measured Evaluation of the Unskewed Ideal Rib Configuration

Fig. 11 shows the simulated and the measured uncoupled flux linkages and inductances of the unskewed ideal rib rotor configuration RSM. The measured results correlate well with the simulated results. More importantly, these results show that this configuration has a high saliency at zero reference current. To confirm this, a simple test is devised to test the drive's PSC capability. The alternating HF injection method is implemented on this drive with a reference current of 0 A, while the IM is used to drive the RSM at a constant speed. It is not possible to control the lateral-rib rotor RSM position sensorless under these conditions due to the small magnitude of the saliency. With the unskewed ideal rib configuration, the HF method tracks the electrical angle effectively, as shown in Fig. 12. A very small q-axis current of 0.04 p.u exists as a result of the HF voltage excitation. No additional q-axis current is thus required to saturate the q-axis flux when no torque is required.

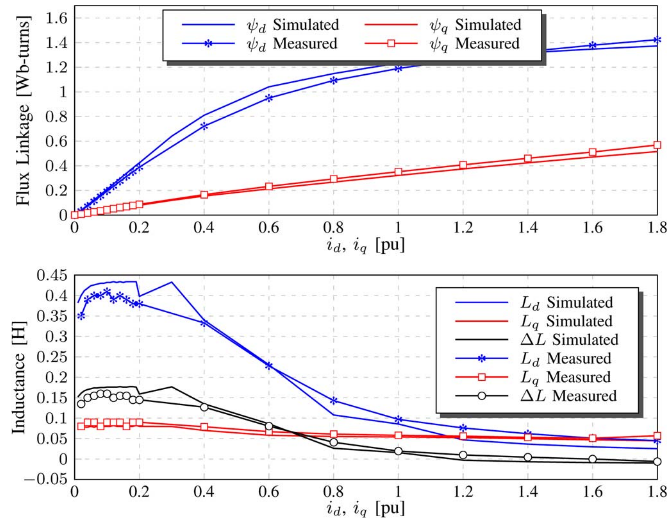

Fig. 11. Simulated versus measured results of the unskewed ideal rib configuration.

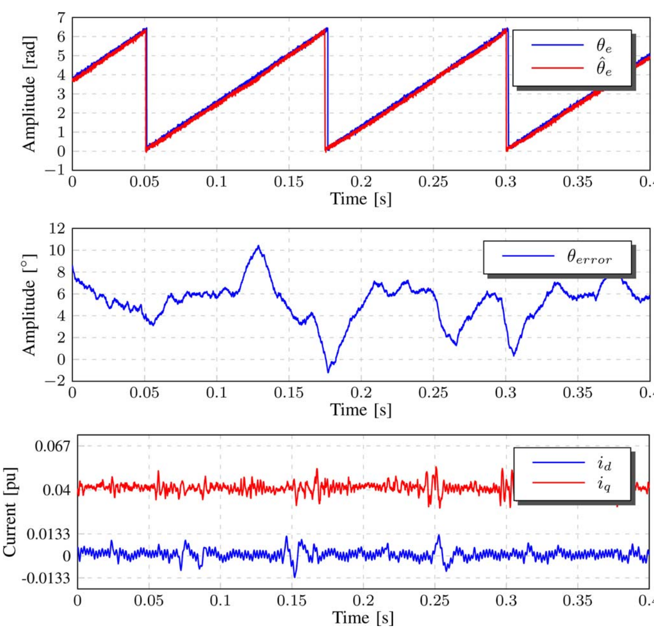

Fig. 12. Measured results of the HF injection method implemented on the unskewed ideal rotor configuration RSM design. Reference current of 0 A while driven by an IM drive at constant speed.

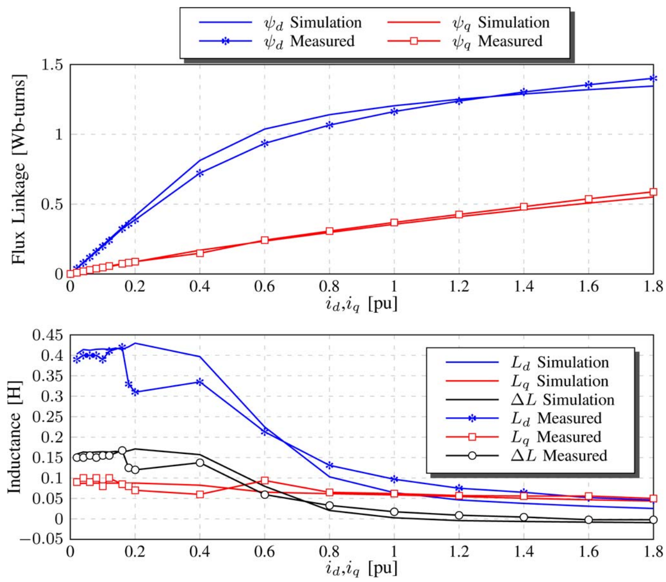

Fig. 13. Simulated versus measured results of the skewed ideal rib configuration.

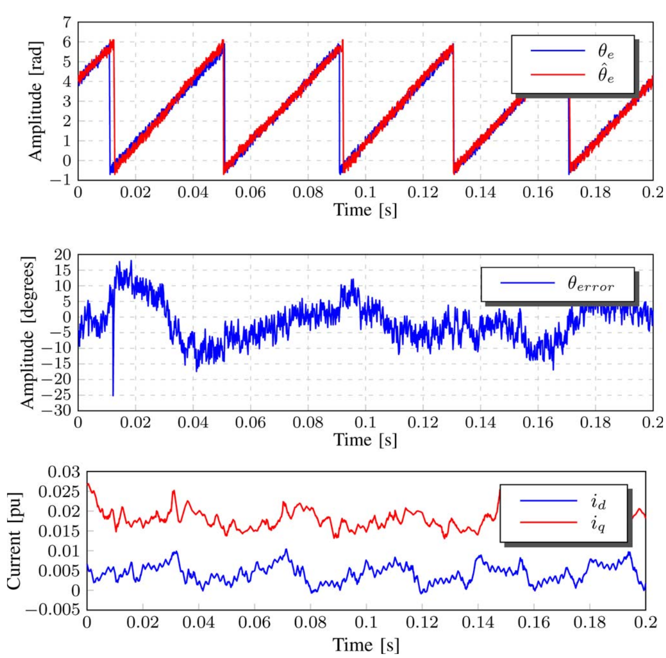

Fig. 14. Measured results of the HF injection method implemented on the skewed ideal rotor configuration RSM. Reference current of 0 A while driven by an IM drive at constant speed.

C. Measured Evaluation of the Skewed Ideal Rib Configuration

The measured and simulated uncoupled flux linkages and inductances of the skewed ideal rotor RSM are shown in Fig. 13. Again, the measured results correlate well with the simulated results. These results show that this configuration has a large-enough saliency to perform position-sensorless control at zero reference current. This is confirmed by the same HF injection test performed on the unskewed rotor. The results of this test in Fig. 14 clearly show that even though the rotor is skewed one slot pitch, PSC is still possible and that a high-enough saliency exists under no-load conditions to estimate the electrical angle.

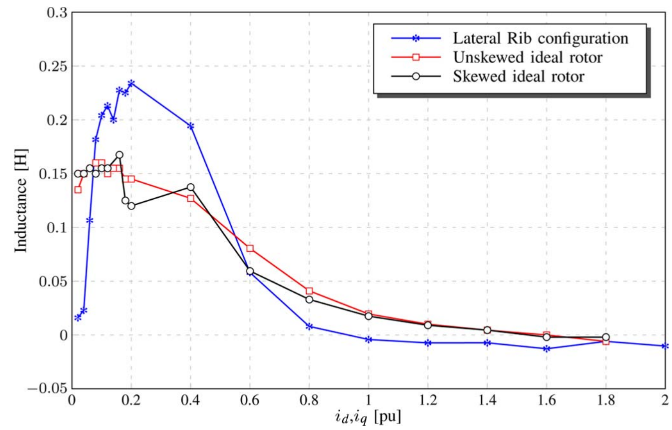

Fig. 15. Measured inductance saliency of the three RSM designs.

D. Concluding Remarks on the Ideal Rotor RSM Construction

No measures were taken to protect a "fragile" rotor design during the testing procedures of the two ideal rotor RSM drives. These two designs underwent harsh testing procedures, most of them at above rated conditions. No damage was caused to the rotor as a result of these tests. It seems that the epoxy–hook combination ensures stability of the rotor. Finally, Fig. 15 compares the measured inductance saliency of the three measured RSM designs. This graph clearly shows that the two ideal rotor configurations have a large saliency at very small and zero current magnitudes as well as a higher saliency under loaded conditions.

IX. Frequency Harmonics of the Fundamental Saliency Position Estimation Error

The purpose is to evaluate if the RSM drive's fundamental saliency PSC capability is affected when the ribs of the lateral-rib rotor RSM is removed. All three position-sensorless controlled RSM drives are evaluated with speed control at 50 Hz at full load. The FFT of the fundamental saliency PSC position estimation error $\Delta\theta_e$ of all three drives under these conditions is displayed in Fig. 16. In [22], it is shown that the fundamental saliency PSC method is dependent on a sufficiently large rotor speed to function properly. It is also shown in [22] that the position estimation error is related to the electrical frequency of the machine. The effect of this phenomenon can be seen in Fig. 16. It is clear that there are large 50-Hz harmonics present in the position estimation error of all three machines in Fig. 16.

In effect, the PLL of the fundamental saliency PSC method proposed in [22] is fed $\Delta\theta_e$, which is speed dependent. Fig. 16 shows that there are two main harmonics present in $\Delta\theta_e$, namely, 25 and 50 Hz. The PLL tracks the 50-Hz harmonic. Furthermore, Fig. 16 shows that the skewed ideal rib rotor RSM has the largest harmonic at 50 Hz and the smallest one at 25 Hz. This might be due to the skewing of the rotor which reduces harmonics in the machine. This graph suggests that it is easier for the fundamental saliency PSC method to track the electrical angle of the skewed ideal rotor RSM due to the reduction of the 25-Hz harmonic in $\Delta\theta_e$. This statement is also confirmed by practical measurement of the three machines.

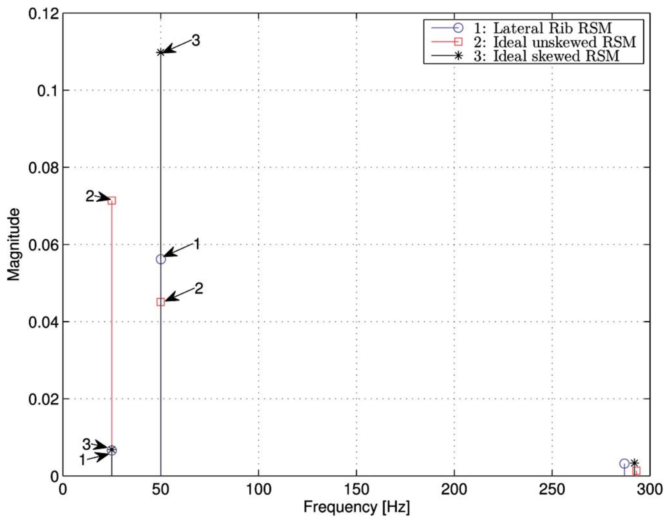

Fig. 16. FFT of fundamental saliency position estimation error signal at 50 Hz under full-load conditions.

TABLE II
MEASUREMENTS OF LATERAL-RIB ROTOR RSM DRIVE

	i [pu]	P_{in} [kW]	P_m [kW]	P_{loss} [kW]	η	PF
Encoder	1.0	1.35	1.14	0.21	84.4%	0.53
Sensorless	1.0	1.35	1.14	0.21	84.4%	0.53

TABLE III
MEASUREMENTS OF THE UNSKEWED IDEAL ROTOR RSM DRIVE

	i [pu]	P_{in} [kW]	P_m [kW]	P_{loss} [kW]	η	PF
Encoder	0.91	1.35	1.16	0.19	85.9%	0.56
Sensorless	0.91	1.36	1.16	0.20	85.2%	0.56

TABLE IV
MEASUREMENTS OF THE SKEWED IDEAL ROTOR RSM DRIVE

	i [pu]	P_{in} [kW]	P_m [kW]	P_{loss} [kW]	η	PF
Encoder	0.93	1.35	1.15	0.20	85.2%	0.58
Sensorless	0.93	1.36	1.15	0.21	84.6%	0.58

X. EFFICIENCY EVALUATION

The UDDS of Fig. 1 display various instances where more or less constant speed is required. It is thus important that an EV drive perform efficiently under these conditions. The three constructed RSM drives are compared in terms of their input (P_{in}) and shaft (P_m) powers in Tables II–IV. It should be noted that none of the evaluated machines are optimized for efficiency. Measurements of the drives are made with a position sensor (encoder) and without (position sensorless). The purpose is to investigate any efficiency loss with PSC.

The digital torque sensor is used to measure the shaft power. The input power of the RSM drives is measured with a digital power analyzer while operating at rated speed. The current and shaft power of the lateral-rib rotor RSM drive (with an encoder) are taken as base values for the purpose of comparison. The currents of the two ideal rib rotor RSM drives are varied during evaluation to obtain a shaft power rating of ± 1.14 kW.

The results in Tables II–IV show that the losses of the three RSM drives when controlled with a sensor are almost identical to the losses when controlled position sensorless. These results then suggest that the losses of the RSMs are the same when controlled with or without a position sensor. Furthermore, these results show that the two ideal rib rotors have a higher torque per ampere rating than the lateral-rib rotor. Tables II–IV show that the efficiency of the two ideal rotor RSM drives are slightly higher than that of the lateral-rib rotor RSM drive. Finally, it is shown that the power factor of the two ideal rotor RSM drives are higher than that of the lateral-rib rotor RSM. The power factor of all three machines, however, are quite low, but this can be improved with proper machine design optimization.

It might be that the removal of the ribs of the lateral-rib rotor RSM causes HF flux pulsations in the iron segments of the rotor. However, no additional losses in the two ideal rib rotor RSM drives have been measured. This aspect must be further investigated, specifically for larger size RSMs.

XI. CONCLUSION

From the FE analysis and measured results of different rotor-structure RSMs, the following conclusions are drawn with regard to the viability of position-sensorless controlled RSMs for VG EV drives.

1) It is shown that the phenomena of saturation and saliency shift that distort saliency-based PSC are not only exclusive to just PM machines but also affect RSMs with lateral-rib rotors, i.e., transverse-laminated rotors with lateral flux barriers and iron ribs.
2) A second PSC problem is identified for lateral-rib rotor RSMs, namely, at zero or very low currents, the magnitude of the saliency is too small for the PSC to estimate the rotor position.
3) However, the inductance saliency of both the unskewed and skewed newly proposed ideal epoxy–resin-casted rotor RSM is found large enough at zero reference current to perform saliency-based PSC. This novel rotor RSM drive also has, as expected, a higher torque per ampere rating than the lateral-rib rotor RSM drive.
4) With regard to rotor skewing, it is found that the inductance saliency of the skewed rotor RSM is almost identical to that of its unskewed counterpart. However, results show that rotor skewing is beneficial when controlled with the fundamental saliency PSC method due to the reduction of harmonics in the position estimation error.
5) An important finding from measurements is that the efficiency of all three position-sensorless controlled RSM drives shows almost no difference in efficiency when controlled with a position sensor.
6) The novel epoxy-casted RSM rotor did not show any damage or problem after heavy drive load laboratory tests. In this regard, the rotor construction can be considered as a viable alternative to the conventional lateral-rib construction. The positive aspects regarding this rotor configuration are highlighted in this paper, yet further investigation is necessary in terms of construction and rotor iron losses.

Overall, it can be concluded that the RSM with a skewed no-iron-rib epoxy-casted rotor experiences no PSC problems from no-load to full-load current and from zero to rated speed. Hence, this makes the RSM with such a rotor as viable and efficient drive motor for automotive and VG EV drives.

Acknowledgment

The authors would like to thank P. Landsmann from TUM for allowing them to use his flux linkage method.

References

[1] Q. Ren, D. Crolla, and A. Morris, "Effect of transmission design on Electric Vehicle (EV) performance," in *Proc. IEEE VPPC*, Sep. 2009, pp. 1260–1265.

[2] A. Sorniotti, M. Boscolo, A. Turner, and C. Cavallino, "Optimization of a multi-speed electric axle as a function of the electric motor properties," in *Proc. IEEE VPPC*, Sep. 2010, pp. 1–6.

[3] L. Lai and M. Ehsani, "Sensitivity analysis of vehicle performance to transmission parameters in parallel HEVs with dynamic programming optimization," in *Proc. IEEE ITEC*, Jun. 2012, pp. 1–5.

[4] T. Hofman and C. Dai, "Energy efficiency analysis and comparison of transmission technologies for an electric vehicle," in *Proc. IEEE VPPC*, Sep. 2010, pp. 1–6.

[5] M. Nashiki, A. Satake, Y. Kawai, T. Yokochi, and S. Okuma, "A new flux-barrier-type reluctance motor with a slit rotor," *IEEE Trans. Ind. Electron.*, vol. 46, no. 6, pp. 1199–1206, Dec. 1999.

[6] J. Germishuizen, F. van der Merwe, K. Van der Westhuizen, and M. Kamper, "Performance comparison of reluctance synchronous and induction traction drives for electrical multiple units," in *Conf. Rec. IEEE IAS Annu. Meeting*, 2000, vol. 1, pp. 316–323.

[7] A. Boglietti, A. Cavagnino, M. Pastorelli, and A. Vagati, "Experimental comparison of induction and synchronous reluctance motors performance," in *Conf. Rec. IEEE IAS Annu. Meeting*, Oct. 2005, vol. 1, pp. 474–479.

[8] N. Bianchi and S. Bolognani, "Influence of rotor geometry of an interior PM motor on sensorless control feasibility," in *Conf. Rec. IEEE IAS Annu. Meeting*, Oct. 2005, vol. 4, pp. 2553–2560.

[9] N. Bianchi, S. Bolognani, and M. Zigliotto, "Design hints of an IPM synchronous motor for an effective position sensorless control," in *Proc. IEEE PESC*, Jun. 2005, pp. 1560–1566.

[10] W. Villet and M. Kamper, "Design of a reluctance synchronous machine for saliency based position sensorless control at zero reference current," in *Proc. IEEE ICIT*, 2013, pp. 301–306.

[11] W. Villet and M. Kamper, "Evaluation of reluctance synchronous machine rotor topologies for position sensorless control," in *Proc. SAUPEC 2013*, Potchefstroom, South Africa.

[12] *US Code of Federal Regulations, Title 40, Part 86, Appendix I*, Code of Federal Regulations (CFR), Jul. 1, 2012, pp. 543–610. [Online]. Available: http://www.dieselnet.com/standards/cycles/ftp72.php

[13] S.-C. Agarlita, I. Boldea, and F. Blaabjerg, "High-frequency-injection-assisted active-flux-based sensorless vector control of reluctance synchronous motors, with experiments from zero speed," *IEEE Trans. Ind. Appl.*, vol. 48, no. 6, pp. 1931–1939, Nov./Dec. 2012.

[14] K. Ide, H. Iura, and M. Inazumi, "Hybrid sensorless control of IPMSM combining high frequency injection method and back emf method," in *Proc. 36th IEEE IECON*, 2010, pp. 2236–2241.

[15] C. Silva, G. Asher, and M. Sumner, "Hybrid rotor position observer for wide speed-range sensorless pm motor drives including zero speed," *IEEE Trans. Ind. Electron.*, vol. 53, no. 2, pp. 373–378, Apr. 2006.

[16] O. Wallmark and L. Harnefors, "Sensorless control of salient PMSM drives in the transition region," *IEEE Trans. Ind. Electron.*, vol. 53, no. 4, pp. 1179–1187, Jun. 2006.

[17] G. Wang, R. Yang, and D. Xu, "DSP-based control of sensorless IPMSM drives for wide-speed-range operation," *IEEE Trans. Ind. Electron.*, vol. 60, no. 2, pp. 720–727, Feb. 2013.

[18] W. Villet, M. Kamper, P. Landsmann, and K. R. , "Hybrid position sensorless vector control of a reluctance synchronous machine through the entire speed range," in *Proc. 15th Int. EPE-PEMC Conf.*, Novi Sad, Serbia, Sep. 2012, pp. LS4b-1.1-1–LS4b-1.1-7.

[19] D. Raca, P. Garcia, D. Reigosa, F. Briz, and R. Lorenz, "A comparative analysis of pulsating vs. rotating vector carrier signal injection-based sensorless control," in *Proc. 23rd IEEE APEC Expo*, Feb. 2008, pp. 879–885.

[20] M. Linke, R. Kennel, and J. Holtz, "Sensorless position control of permanent magnet synchronous machines without limitation at zero speed," in *Proc. 28th IEEE IECON*, 2002, vol. 1, pp. 674–679.

[21] W. Hammel and R. Kennel, "Position sensorless control of PMSM by synchronous injection and demodulation of alternating carrier voltage," in *Proc. 1st Symp. SLED*, Jul. 2010, pp. 56–63.

[22] P. Landsmann, R. Kennel, H. de Kock, and M. Kamper, "Fundamental saliency based encoderless control for reluctance synchronous machines," in *Proc. 19th ICEM*, Sep. 2010, pp. 1–7.

[23] N. Bianchi, S. Bolognani, J.-H. Jang, and S.-K. Sul, "Comparison of PM motor structures and sensorless control techniques for zero-speed rotor position detection," *IEEE Trans. Power Electron.*, vol. 22, no. 6, pp. 2466–2475, Nov. 2007.

[24] J. Arellano-Padilla, C. Gerada, G. Asher, and M. Sumner, "Inductance characteristics of PMSMs and their impact on saliency-based sensorless control," in *Proc. 14th Int. EPE/PEMC Conf.*, Sep. 2010, pp. S1-1–S1-9.

[25] C. Gerada, J. Padilla, M. Sumner, and T. Raminosoa, "Loading effects on saliency based sensorless control of PMSMs," in *Proc. ICEMS*, Nov. 2009, pp. 1–6.

[26] P. Guglielmi, M. Pastorelli, and A. Vagati, "Impact of cross-saturation in sensorless control of transverse-laminated synchronous reluctance motors," *IEEE Trans. Ind. Electron.*, vol. 53, no. 2, pp. 429–439, Apr. 2006.

[27] N. Bianchi and S. Bolognani, "Sensorless-oriented design of PM motors," *IEEE Trans. Ind. Appl.*, vol. 45, no. 4, pp. 1249–1257, Jul./Aug. 2009.

[28] R. Wrobel, A. S. Budden, D. Salt, D. Holliday, P. Mellor, A. Dinu, P. Sangha, and M. Holme, "Rotor design for sensorless position estimation in permanent-magnet machines," *IEEE Trans. Ind. Electron.*, vol. 58, no. 9, pp. 3815–3824, Sep. 2011.

[29] P. Sergeant, F. De Belie, and J. Melkebeek, "Rotor geometry design of interior PMSMs with and without flux barriers for more accurate sensorless control," *IEEE Trans. Ind. Electron.*, vol. 59, no. 6, pp. 2457–2465, Jun. 2012.

Wikus T. Villet (S'12) received the B.Eng. degree in electrical and electronic engineering from the University of Stellenbosch, Stellenbosch, South Africa, in 2010, where he is currently working toward the Ph.D. (Eng.) degree in the Department of Electrical and Electronic Engineering. His current research focuses on position-sensorless control methods of reluctance synchronous machine drives.

Maarten J. Kamper (SM'08) received the M.Sc. (Eng.) degree and the Ph.D. (Eng.) degree from the University of Stellenbosch, Stellenbosch, South Africa, in 1987 and 1996, respectively.

He has been with the academic staff of the Department of Electrical and Electronic Engineering, University of Stellenbosch, since 1989, where he is currently a Professor of Electrical Machines and Drives. His research interests include computer-aided design and control of reluctance, permanent-magnet, and induction machine drives.

Prof. Kamper is a South African National Research Foundation-supported scientist and a Registered Professional Engineer in South Africa.